ACS OMEGA

http://pubs.acs.org/journal/acsodf

Article

Low-Temperature Selective Catalytic Reduction of NO_x with NH_3 over Mn−Ce Composites Synthesized by Polymer-Assisted Deposition

Xixi Xiao, Jitong Wang,* Xianfeng Jia, Cheng Ma, Wenming Qiao,* and Licheng Ling

Cite This: *ACS Omega* 2021, 6, 12801−12812

Read Online

ABSTRACT: The Mn_xCe_y binary catalysts with a three-dimensional network structure were successfully prepared via a polymer-assisted deposition method using ethylenediaminetetraacetic acid and polyethyleneimine as complexing agents. The developed pore structure could facilitate the gas diffusion and accelerate the catalytic reaction for NH_3 selective catalytic reduction (SCR). Moreover, the addition of Ce is beneficial for the exposure of active sites on the catalyst surface and increases the adsorption of the NH_3 and NO species. Therefore, the Mn_1Ce_1 catalyst exhibits the best catalytic activity for NO_x removal with a conversion rate of 97% at 180 °C, superior water resistance, and favorable stability. The SCR reaction over the Mn_1Ce_1 catalyst takes place through the E−R pathway, which is confirmed by the in situ diffuse reflectance Fourier transform analysis. This work explores a new strategy to fabricate multimetal catalysts and optimize the structure of catalysts.

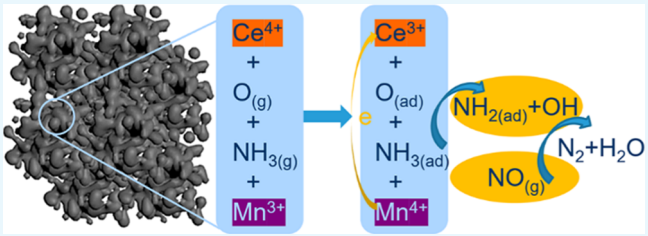

1. INTRODUCTION

Nitrogen oxides (NO_x, standing for NO and NO_2) are among the most harmful air pollutants which can lead to the formation of acid rain, photochemical fumes, ozone depletion, and climate change.[1−3] Governments and related institutions have paid considerable attention to reducing the emission of NO_x from vehicle exhaust and electric power plants.[4,5] NH_3 selective catalytic reduction (NH_3-SCR) of NO_x has been considered as an advanced technology for the elimination of nitrogen oxides from coal-fired power plants owing to the low cost and high efficiency.[6,7] At present, in the field of fixed source denitrification, the V_2O_5/TiO_2 catalyst has attracted extensive interest due to its good selectivity, high catalytic activity at 260−450 °C, stable properties, anti-poisoning ability, and strong anti-aging performance.[8−13] Despite these considerable advantages, there are still some problems including narrow window of operation temperature, biological toxicity, and increasing energy consumption, which have impeded the practical application of the V_2O_5−WO_3 (MoO_3)/TiO_2 catalyst system.[14−16]

In recent decades, researchers have investigated varieties of low-temperature denitrification catalysts, including transition metal oxide catalysts, precious metal catalysts, and ion-exchange molecular sieve catalysts.[17−19] Typically, the low-cost transition metal catalyst shows good SCR activity and high selectivity in the low-temperature range, such as Mn/TiO_2, Cu/TiO_2, Co/TiO_2, Ni/TiO_2, Ce/TiO_2, $FeTiO_x$, V_2O_5/WO_3−TiO_2, Ce−Fe−Ti, Ce−W−Ti, Fe−V−Ti, and WO_3/TiO_2.[20−22] Among them, manganese-containing composite catalysts have emerged as a promising candidate owing to their excellent activity for SCR reaction.[23] Particularly, the MnO_x−CeO_2 composite has been reported to be active at the low-temperature SCR of NO_x (100−200 °C).[24] Qi et al. synthesized MnO_x−CeO_2 composite oxides by a co-precipitation method, which showed high NO_x conversion at low temperature.[25] Tang et al. found that a MnO_x−CeO_2/AC/C composite exhibited 78% NO conversion at 100 °C.[26] Li et al. reported that after doping CeO_2 with MnO_x, MnO_x−CeO_x can enhance the de−NO_x conversion, H_2O resistance, and stability.[27] The morphology and structure of the MnO_x−CeO_2 composite are of great significance in the low-temperature SCR process, which has a crucial effect on the dispersion and oxidation state of manganese.[28−30] Guo et al. prepared a CeO_x@MnO_x core−shell structure catalyst by using a citric acid method, which was of high intrinsic catalytic activity derived from the core−shell structure.[31] However, the complicated multistep reaction processes and the introduction of templates make it difficult to be practically used on a large scale.

It has been demonstrated that the synthesis methods also have a critical impact on the physicochemical properties and

Received: March 2, 2021
Accepted: April 16, 2021
Published: May 3, 2021

catalytic performance of redox catalysts.[32−34] Recently, polymer-assisted deposition, an aqueous chemical route, has been developed to prepare multicomponent metal oxides using polyethyleneimine (PEI) and ethylenediaminetetraacetic acid (EDTA) as complexing agents.[35] In the polymer-assisted deposition process, metal ions bound to polymers are used as reaction precursors. The formation of a covalent complex between the nitrogen atoms and the metal precursors of multidentate polymers makes it possible to prepare most metal precursor solutions, which is not available to obtain through commonly used chemical solution deposition techniques. Multicomponent metal oxide networks could be obtained, with oxide nanoparticles uniformly dispersed in the framework. This low-cost chemical solution approach offers a new opportunity for the development of binary metal oxides. However, there are no reports on using the polymer-assisted deposition method to synthesize Mn_xCe_y binary catalysts for selective catalytic reduction of NO_x.

In this work, a series of Mn_xCe_y binary catalysts with nanostructures are prepared through the polymer-assisted deposition method. The polymers could not only form an initial network but also inhibit the aggregation of metal oxide particles, enabling the generation of a uniform solution. Mn_xCe_y binary catalysts with a three-dimensional (3D) network composed of uniformly dispersed metal oxide nanoparticles could be obtained after heat treatment. The well-developed mesopore and macropore structure could facilitate the diffusion of reaction gas and exposure of active sites of the catalyst. MnO_x nanoparticles with uniform size are well dispersed in the framework, which serve as the catalytic oxidation center, while the formation of cerium-based solid solution could provide more active sites for catalytic oxidation. In addition, with excellent oxygen storage capacity, CeO_2 could function as an oxygen reservoir and oxygen supplier during the catalytic process. Therefore, the Mn_xCe_y binary catalysts demonstrate high catalytic activity for low-temperature catalytic reduction of NO_x with NH_3. This is the first attempt to adopt the polymer-assisted deposition route for the fabrication of Mn_xCe_y binary oxides as catalysts in the catalytic reduction of NO_x. This simple chemical solution strategy opens up a new way for the design and construction of multicomponent metal oxides used for low-temperature SCR of NO_x with NH_3.

2. EXPERIMENTAL SECTION

2.1. Catalyst Preparation. Binary oxides Mn_xCe_y (x = 2, 1.5, 1, and 0.5, y = 1) were prepared by polymer-assisted deposition route by using EDTA and PEI as binding ligands.[36] In a typical synthesis of Mn_1Ce_1, 1.07 g of $Mn(NO_3)_2$ (50 wt %, Sinopharm), 1.30 g of $Ce(NO_3)_2{\cdot}6H_2O$ (99%, Macklin), 3.00 g of EDTA (99%, Acros Organics), and 3.00 g of PEI (Mw-800, Aldrich) were dissolved in 60 mL of deionized water under vigorous stirring to obtain a transparent and clear precursor solution. Then, the above solution was placed in an 80 °C oven until water was evaporated to form a transparent solid. The obtained dry gel was calcined in the air with a ramping speed of 1 °C/min and then maintained at 500 °C for 4 h. Finally, the catalyst can be obtained after cooling naturally to room temperature. The MnO_x catalyst can be produced when no cerium source is added. The amount of $Ce(NO_3)_2{\cdot}6H_2O$, EDTA, and PEI was fixed at 1.30, 3.00, and 3.00 g, respectively, while the amount of $Mn(NO_3)_2$ was controlled at 2.15, 1.60, 1.07, and 0.85 g, corresponding to the Mn/Ce molar ratio of 2, 1.5, 1, and 0.5. The as-prepared binary oxide catalyst was marked as Mn_xCe_y (x = 2, 1.5, 1, and 0.5, y = 1). For comparison, the Mn_1Ce_1-co-precipitation method (CP) composite was prepared by a traditional CP.[37]

2.2. Catalyst Characterization. The morphologies and microstructures of the as-prepared Mn_xCe_y were examined by scanning electron microscopy (SEM, Gemini SEM 500), transmission electron microscopy (TEM, JEOL, JEM-2100), and field-emission TEM. The energy-dispersive X-ray spectrometry (EDS) mappings of the selected region were acquired on an energy-dispersive X-ray spectrometer attached to the SEM instrument (Nova Nano SEM 450).

The X-ray diffraction (XRD) patterns were recorded on a rotating anode X-ray powder diffractometer operated on a RigakuD/MAX 2550 diffractometer with Cu Kα radiation. Intensity data was collected over a 2 range of 10−80° with a step size of 0.05° and an accumulation time of 1 s per step.

The Raman spectra were recorded on a laser micro-Raman spectrometer (≤I0.2/cm/invia reflex) equipped with laser supplying the excitation line at 532 nm. The spectrometer was calibrated using the silicon line at 521 cm^{-1}.

The nitrogen adsorption−desorption isotherms were conducted at 77 K on a QUADRASORB SI analyzer. The samples were first degassed under vacuum at 120 °C for 10 h before measurement. The specific surface areas and average pore diameters were determined using the Brunauer−Emmett−Teller (BET) equation and the Barrett−Joyner−Halenda (BJH) model from the desorption branch, respectively.

Hydrogen temperature-programmed reduction (H_2-TPR) and NH_3 temperature-programmed desorption (NH_3-TPD) were performed on a Chem BET Pulsar (Automated Chemisorption analyzer) equipped with a TCD detector. For the H_2-TPR, the sample was first pretreated in He (120 mL/min) at 200 °C for 40 min and then cooled to room temperature. Subsequently, the sample was heated up to 800 °C at a rate of 10 °C/min under H_2 (120 mL/min). For NH_3-TPD, 50 mg of sample powder was weighed and pretreated at 200 °C for 30 min in a flow of He (120 mL/min). After cooling to room temperature, the adsorption gas was saturated with NH_3 for 60 min. After saturation, the sample was rinsed in pure He flow for 30 min. Finally, the sample was heated to 800 °C at a heating rate of 5 °C/min.

The surface atomic states of the catalysts were determined by X-ray photoelectron spectroscopy (XPS, ESCALAB 250Xi) using Al Kα radiation ($h\nu$ = 1486.6 eV). The binding energies were calibrated using the C 1s peak at 284.6 eV as a reference and the peak deconvolution was carried out using the XPS Speak software.

In situ diffuse reflectance Fourier transform spectroscopy (DRIFTS) measurements were conducted on a Fourier transform infrared spectrometer (PerkinElmer, Model Spectrum 100) and an in situ cell (modified Harricks Model HV-DR2) with a mercury cadmium telluride detector cooled using liquid N_2. The gas flow was controlled at 100 mL/min by the mass flow meter. Before the gas adsorption experiment, the sample was pretreated in nitrogen at 300 °C for 1 h to blow away the impurities. The corresponding background spectra were recorded and subjected to a subtraction process from the sample spectrum. The experimental atmosphere for in situ DRIFTS study was as follows: 500 ppm NH_3/N_2 or/and 500 ppm NO/N_2 + 5 vol % O_2/N_2.

2.3. Catalytic Activity Test. The SCR catalytic performance was carried out in a fixed-bed reactor with an internal

https://doi.org/10.1021/acsomega.1c01123
ACS Omega 2021, 6, 12801−12812

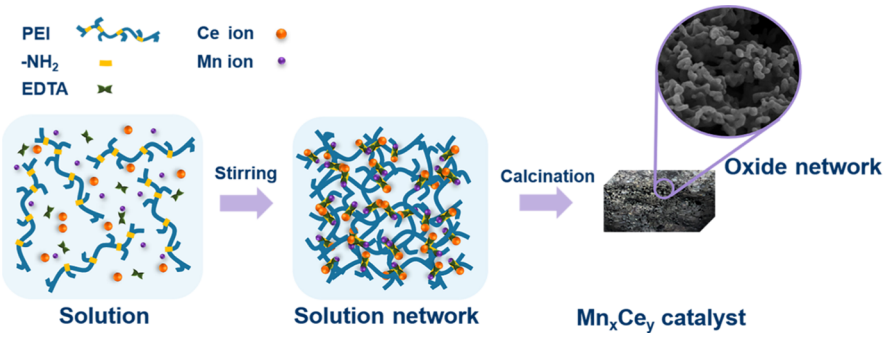

Figure 1. Schematic of the synthesis of the bimetal oxide network by the polymer-assisted deposition approach.

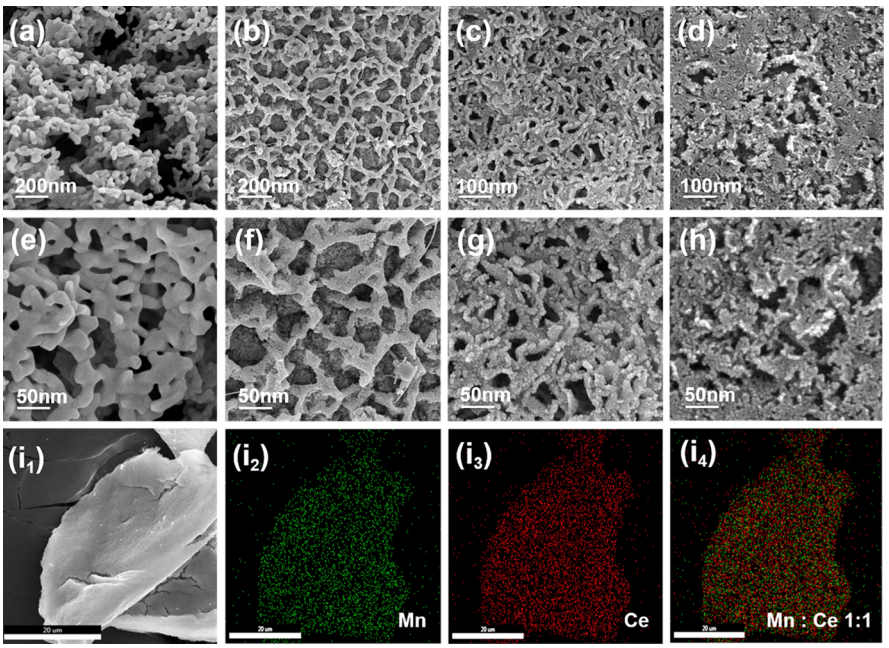

Figure 2. SEM images and EDS mappings of Mn_xCe_y binary catalysts: (a,e) SEM images of MnO_x; (b,f) Mn_2Ce_1; (c,g) Mn_1Ce_1; (d,h) $Mn_{0.5}Ce_1$; and (i_{1-4}) EDS mappings of Mn_1Ce_1.

diameter of 10 mm. The temperature of the fixed-bed column was controlled by an electric heating furnace. The catalyst of 100 mg was sandwiched between the quartz cotton in the quartz tube. The simulated fumes were introduced into the reactor. The flow of simulated flue gas was controlled by a mass flow meter, which consisted of 500 ppm NO, 5 vol % O_2, 500 ppm NH_3, and N_2 balance gas. In all reaction activity evaluation experiments, the total gas flow was 500 mL/min, with a gas hourly space velocity (GHSV) of 38,000 h^{-1}, and the reaction temperature was controlled at 60−300 °C. The stationary state NO_x conversion and N_2 selectivity of the sample can be calculated according to the following formulas

$$NO_{x\ \mathrm{conversion}} = (NO_{x,\mathrm{in}} - NO_{x,\mathrm{out}})/NO_{x,\mathrm{in}} \times 100\%$$

$$N_{2\ \mathrm{selectivity}} = (1 - (NO_{2,\ \mathrm{out}} + 2N_2O_{\mathrm{out}}) / (NO_{x,\mathrm{in}} + NH_{3,\mathrm{in}})) \times 100\%$$

In the formula, $NO_{x,\mathrm{in}}$, $NO_{x,\mathrm{out}}$, $NO_{2,\mathrm{out}}$, N_2O_{out}, and $NH_{3,\mathrm{in}}$ indicated the inlet and outlet concentrations at steady state, respectively.

3. RESULTS AND DISCUSSION

3.1. Material Characterization. The Mn_xCe_y binary networks were synthesized by the polymer-assisted deposition method (Figure 1). The dissolved polymers could serve not only as the initial network during the reaction process but also as a binding agent to bond with the metal ions, facilitating homogeneous dispersion of the metal oxide. After drying and calcination, EDTA and PEI decomposed to produce gases which escape from the system, remaining a bimetal oxide interconnected network with a porous structure originated from the organic polymer structure.

The morphology and structure of the mixed bimetal oxide networks were revealed by SEM and EDS mappings. As can be seen from Figure 2, the four samples are all composed of 3D porous structures formed by crosslinking of metal oxide nanoparticles. The coordination of metal ions with the polymer could enable the uniform distribution of metal ions and prevent their aggregation, resulting in a small particle size. Moreover, the particle size decreases from 25 to 3 nm with the decreasing Mn/Ce molar ratio. Compared with Mn_2Ce_1, Mn_1Ce_1 shows a tighter network structure, suggesting higher specific surface area and more exposed active sites. As the Mn/Ce molar ratio decreases to 0.5, excess cerium causes

https://doi.org/10.1021/acsomega.1c01123
ACS Omega 2021, 6, 12801−12812

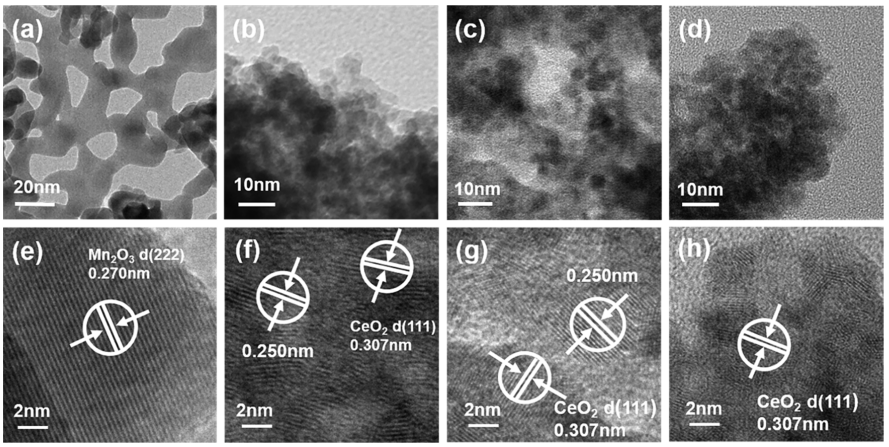

Figure 3. TEM (a−d) and HRTEM (e−h) images of the mixed oxide networks: (a,e) MnO_x; (b,f) Mn_2Ce_1; (c,g) Mn_1Ce_1; and (d,h) $Mn_{0.5}Ce_1$.

deformation and collapse of the 3D network due to the agglomeration of cerium oxides.

The morphology of Mn_xCe_y binary networks was further investigated by TEM as shown in Figure 3. The addition of Ce transforms the loose lattice interface of MnO_x into a dense structure, while the particle size of metal oxides is greatly reduced. Combined with SEM images, the particle size of MnO_x is about 25 nm, whereas the diameter of Mn_xCe_y nanoparticles is as small as 3 nm. Figure 3e−h exhibits the high-resolution TEM (HRTEM) images of Mn_xCe_y. The morphology of metal oxides in the catalyst can be inferred by measuring the lattice spacing. It is found that the lattice spacing of Mn in MnO_x is 0.270 nm, corresponding to the Mn_2O_3(222) plane, which indicates that the valence state of Mn in the MnO_x catalyst is Mn^{3+}.[38] In the Mn_xCe_y catalyst, the lattice spacing of 0.307 nm is related to the CeO_2(111) surface.[39] In addition, the presence of 0.250 nm lattice spacing may be due to the replacement of Mn with a similar but smaller ion radius in the cubic fluorite structure, which causes decrease of the lattice spacing.[40]

The results obtained from the XRD analysis of Mn_xCe_y catalysts are presented in Figure 4. A sharp characteristic peak

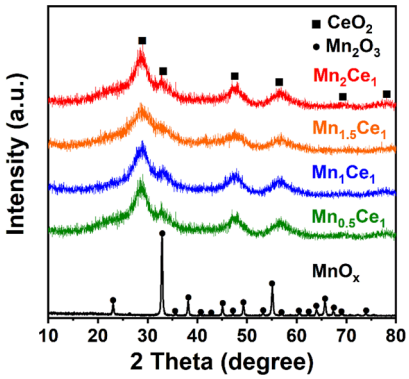

Figure 4. XRD patterns of the Mn_xCe_y binary catalysts.

of MnO_x is observed corresponding to α-Mn_2O_3 (JCPDS 31-825), indicating that manganese in the MnO_x catalyst is in the form of Mn_2O_3 which is consistent with the HRTEM result. The XRD analysis patterns for all the bimetal oxides with different proportions are basically the same. No strong or sharp peak of MnO_x is observed while only the broad diffraction peaks representing CeO_2 can be seen, which suggests that a Mn−Ce solid solution is formed. It has been reported that when Mn/(Mn + Ce) < 0.5, the XRD analysis pattern only had the wide peak of CeO_2, indicating the presence of Mn−Ce solid solution.[41] In addition, it has been reported that when a metal ion is successfully incorporated into the CeO_2 lattice, the XRD peak corresponding to the oxide of that metal is not observed, which also resembles the above result.[42]

The Raman spectra of the samples are shown in Figure S1. The bands at 338−360 and 632−649 cm^{-1} can be associated with the out-of-plane bending mode of α-Mn_2O_3 nanocrystals.[43] As for Mn_xCe_y, the peaks centered on 446, 458, and 460 cm^{-1}, which belong to the triple degenerated F_{2g} active mode, are typical fluorine-like cerium structures.[44] However, it is worth mentioning that the CeO_2 and Mn_2O_3 vibration peaks shift to lower intensity with the decrease of Mn/Ce molar ratio, and the peak at 300−400 cm^{-1} even disappears on $Mn_{0.5}Ce_1$. This indicates that manganese is integrated into the crystal lattice of CeO_2 and the adding of cerium species inhibits the crystallization of Mn_2O_3 at the same time.[45,46]

The pore structures of the MnO_x and bimetal oxide networks were measured by N_2 isothermal adsorption/desorption, and the resultant pore parameters are listed in Table 1. The N_2 adsorption and desorption isotherms of the

Table 1. Pore Parameters of the Mn_xCe_y Binary Catalysts

sample	S_{BET}[a] (m^2 g^{-1})	V_t[b] (cm^3 g^{-1})	D_p[c] (nm)
MnO_x	23.0	0.08	6.1
Mn_2Ce_1	75.7	0.13	3.1
$Mn_{1.5}Ce_1$	87.7	0.11	3.1
Mn_1Ce_1	113.2	0.20	3.5
$Mn_{0.5}Ce_1$	107.4	0.18	3.5

[a]Specific surface area. [b]Total pore volume. [c]Average pore diameter.

four samples in Figure S2 show the IUPAC type IV mode with obvious hysteresis loops, suggesting the existence of mesoporous structures.[47] For the raw MnO_x, the BET surface area is only 23.0 m^2 g^{-1} with a pore volume of 0.08 cm^3 g^{-1}. As for Mn_xCe_y binary networks, an increasing trend of pore structure with the decreasing Mn/Ce molar ratio is noted for the samples, owing to the formation of a highly dispersed Mn−Ce composite.[48] The surface area and pore volume of Mn_1Ce_1 increase to 113.2 m^2 g^{-1} and 0.20 cm^3 g^{-1}, respectively. The average pore size calculated by the BJH method declines to 3.5 nm, which is attributed to the smaller particle size compared

https://doi.org/10.1021/acsomega.1c01123
ACS Omega 2021, 6, 12801−12812

with MnO_x. The addition of Ce can reduce the size of the metal oxide particles and increase the specific surface area of the catalyst, which is beneficial to the exposure of active sites on the catalyst surface. When further decreasing the Mn/Ce molar ratio, the BET surface area decreases slightly owing to the aggregation of metal oxide particles.

Previous studies have reported that the catalytic performance is related to the redox performance of the catalyst in the NH_3-SCR process.[49] The reduction pattern of the Mn_xCe_y binary metal catalysts was recorded by using H_2-TPR. The corresponding TPR profiles are presented in Figure 5. The

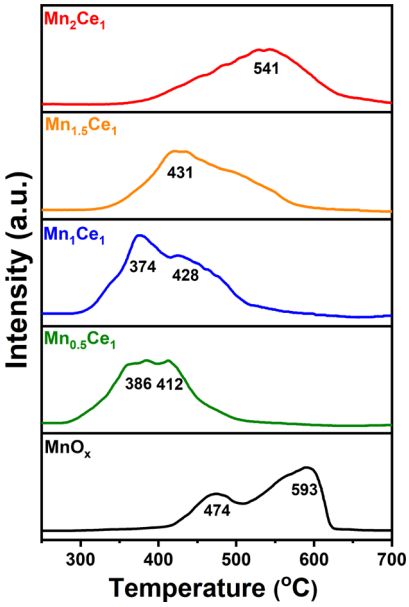

Figure 5. H_2-TPR patterns of Mn_xCe_y binary catalysts.

reduction peaks at 474 and 593 °C are observed in the MnO_x catalyst, which are related to the reduction of Mn_2O_3 to Mn_3O_4 and the reduction of Mn_3O_4 to MnO, respectively.[50,51] Compared with MnO_x, the reduction peaks of Mn_xCe_y shift toward lower temperature range (370−550 °C). In the case of Mn_2Ce_1 and $Mn_{1.5}Ce_1$, only one reduction peak can be seen at 541 and 431 °C, respectively. However, with the decrease of Mn/Ce molar ratio, Mn_1Ce_1 and $Mn_{0.5}Ce_1$ present two overlapping peaks with temperature lower than 430 °C. It is difficult to associate the peak with the reduction of different MnO_x species or a specific reduction step of CeO_2 because the reduction of Mn and Ce ion occurs simultaneously.[52,53] The reduction peak of the Mn_xCe_y catalyst shifts to a lower temperature range compared to the MnO_x catalyst, indicating fairly easy reducibility.[54,55] This suggests that the Mn−Ce composite effectively enhances the storage and transfer of active oxygen and advances the catalytic cycle during the SCR process.[56] Moreover, the developed pore structure enhances the gas molecule diffusion inside the catalyst, which may be beneficial to the catalytic reaction.

The acid sites on the SCR catalyst surface determine the adsorption and activation ability of NH_3 on the catalyst surface. The results of the NH_3-TPD desorption study are displayed in Figure 6. The analytical peak at high temperatures belongs to Lewis acid sites, and the analytical peak below 200 °C belongs to Brønsted acid sites.[57] The curve of pure MnO_x only has an essential Lewis acid sites as shown in Figure 6. The peak intensity of Mn_xCe_y catalysts is stronger than that of pure

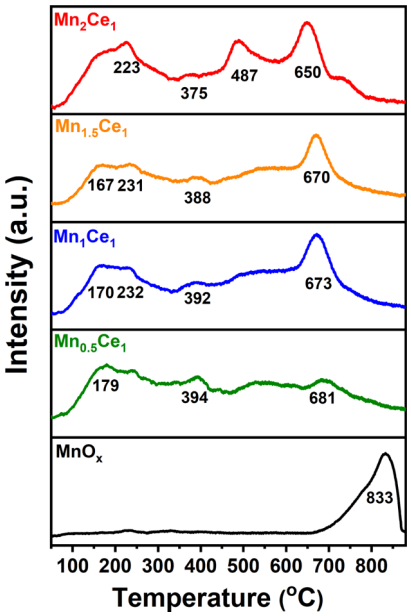

Figure 6. NH_3-TPD patterns of Mn_xCe_y binary catalysts.

MnO_x, which may be ascribed to the higher surface area of these materials. It is interesting to note that the NH_3-desorption peaks monotonically shift to high temperatures with a decrease in Mn/Ce molar ratio. However, although $Mn_{0.5}Ce_1$ exhibits the highest acid site temperature, its peak intensity is relatively smaller compared with that of other samples. This means the total amount of adsorbed NH_3 for $Mn_{0.5}Ce_1$ is lower than that of others (Table 2). The analytic

Table 2. NH_3 Adsorption Amounts of the Mn_xCe_y Binary Catalysts

catalyst	NH_3 adsorption amount (mmol/g)
MnO_x	0.8
Mn_2Ce_1	1.8
$Mn_{1.5}Ce_1$	1.7
Mn_1Ce_1	2.2
$Mn_{0.5}Ce_1$	1.5

peak temperature of Mn_1Ce_1 is higher than the ones of other Mn_xCe_y samples, indicating that there is a larger number of acid sites. Higher NH_3 adsorption capacity at Brønsted acid sites is beneficial to the NH_3-SCR process at low temperature. Compared with Brønsted acid sites under similar conditions, Lewis acid centers have been revealed to maintain high NO conversion and low N_2O formation.[58] Mn_2Ce_1 shows a new analytic peak at 487 °C. This suggests that different Mn/Ce ratios have an influence on the acid position distribution and concentration of the catalyst. Enhancing the acid site distribution of Mn_xCe_y binary catalysts is conducive to improving the adsorption capacity of ammonia, which has significant benefits for improving de-NO_x ability.[59]

To determine the atomic concentration on the catalyst surface and further obtain the valence states of Mn and Ce in the Mn_xCe_y binary metal oxide, XPS analysis was performed. High-resolution spectra of Mn 2p, Ce 3d, and O 1s are presented in Figure 7. The Ce 3d spectrum of the Mn_xCe_y binary metal oxide catalyst is displayed in Figure 7a. By conducting peak-fitting deconvolution, the Ce 3d XPS spectrum could be separated into eight peaks including v

https://doi.org/10.1021/acsomega.1c01123
ACS Omega 2021, 6, 12801−12812

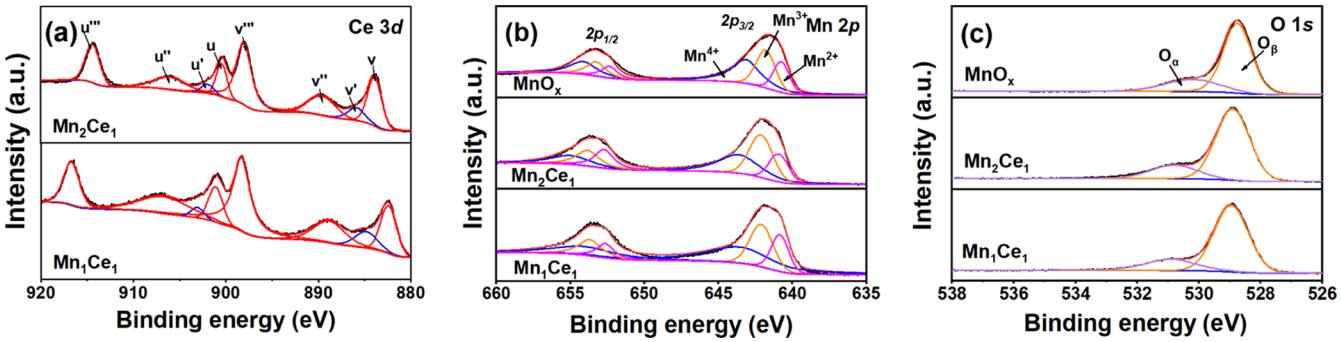

Figure 7. XPS spectra of Mn_xCe_y binary catalysts (a) Ce 3d, (b) Mn 2p, and (c) O 1s.

(882.4 eV), v' (885.3 eV), v'' (888.8 eV), v''' (898.3 eV), u (901.1 eV), u' (903.5 eV), u'' (906.7 eV), and u''' (916.7 eV). It can be seen from the Ce 3d XPS spectrum that the peak "v" corresponds to the Ce $3d_{5/2}$ spin−orbit component, and the peak "u" is related to the Ce $3d_{3/2}$ spin−orbit component. Among them, six peaks of v, v'', v''', u, u'', and u''' (red curve) are consistent with the spectrum of Ce^{4+}, indicating that the main morphology of Ce in Mn_xCe_y binary oxide is CeO_2, while v' and u' (blue curve) can be attributed to the surface Ce^{3+} atoms. Ce 3d XPS results reveal that Ce^{3+} and Ce^{4+} coexist in the manganese−cerium mixed system. In addition, the relative content of Ce^{3+} on the surface is evaluated and listed in Table 3. The superior ratio of Ce^{3+}/Ce^{4+} has been proven to cause oxygen vacancies, charge imbalance, and unsaturated chemical bonds on the catalyst surface, which are conducive to the formation of chemically adsorbed oxygen on the catalyst surface.[60]

Table 3. Concentrations of the Atoms Obtained by XPS Analysis

catalyst	Mn^{4+}/Mn^{3+}	Ce^{3+}/Ce^{4+}	$O_\alpha/(O_\alpha + O_\beta)$
MnO_x	1.28	/	0.29
Mn_2Ce_1	1.45	0.10	0.69
Mn_1Ce_1	1.57	0.11	0.71

The XPS spectra of Mn 2p are displayed in Figure 7b. The overlapping Mn $2p_{3/2}$ signal could be divided into three peaks, which correspond to Mn^{2+} (640.4 ± 0.2 eV), Mn^{3+} (641.3 ± 0.2 eV), and Mn^{4+} (642.1 ± 0.2 eV), respectively. The multiple valence states of Mn in the binary metal oxide catalyst make it easy to alter between valence states, promoting the transfer of electrons during the redox reaction and further boosting the catalytic oxidation performance of the catalyst. Previous work has reported that Mn^{4+} plays a dominant role in accelerating the oxidation of NO to NO_2 in de-NO_x activity.[8] Thus, the relative percentage of Mn^{3+} and Mn^{4+} is calculated from the area of the corresponding characteristic peak and listed in Table 3. The surface Mn^{4+} content of Mn_1Ce_1 is higher than that of MnO_x and Mn_2Ce_1, owing to the electronic interactions between MnO_x and CeO_2, resulting in an improved catalytic performance.

The peak-fitting O 1s XPS spectra for the investigated materials are presented in Figure 7c, which involve two categories: chemically adsorbed oxygen (or weakly chemically bonded oxygen, expressed as O_α, binding energy is located at 531.6−532.0 eV) and lattice oxygen (expressed as O_β, binding energy is located at 529.4−529.7 eV). It has been proved from many literature studies that the chemically adsorbed oxygen on the surface possesses better catalytic activity than lattice oxygen owing to its higher mobility. Therefore, the presence of a high $O_\alpha/(O_\alpha + O_\beta)$ ratio is conducive to the oxidation of NO to NO_2, which promotes the low-temperature activity through the "fast SCR" reaction. The relative atomic percentage of these oxygen species on the catalyst surface can be estimated from the relative areas of these sub-peaks, and the results are summarized in Table 3. It could be seen that the introduction of Ce significantly increases the concentration ratio of O_α, especially for Mn_1Ce_1 with a higher chemisorbed oxygen content of 71%.

3.2. Catalytic Performance. Figure 8a displays the SCR catalytic activity of catalysts with different Mn/Ce molar ratios. The pristine MnO_x shows low catalytic activity with the highest NO conversion of only 59%. Compared with MnO_x, doping of Ce remarkably increases the NO conversion within the whole temperature range owing to the synergistic effect of MnO_x and CeO_2. It can be observed that the NO conversion on all catalysts increases first and then declines slightly with increasing temperature. The SCR activity falls in the following order: Mn_1Ce_1 > Mn_2Ce_1 > $Mn_{1.5}Ce_1$ > $Mn_{0.5}Ce_1$ > MnO_x. The Mn_1Ce_1 exhibits the highest catalytic activity of 97% at 180 °C. This phenomenon reveals that the addition of Ce effectively improves the microstructure and catalytic performance of the catalyst.[29] The significantly reduced metal oxide particle size and increased catalyst-specific surface area are conducive to the exposure of active sites on the catalyst surface, enhancing the adsorption and condensation of NH_3 molecules in the gas phase. Finally, the contact between the reactant molecule and active sites are improved, which is beneficial to the catalytic performance of the catalyst. Nevertheless, the addition of excessive cerium leads to deformation of the 3D network and agglomeration of metal oxide particles, which causes active sites to be covered and the decreased catalytic activity. As a result, the Mn_1Ce_1 catalyst is selected as a representative for further research. The effect of calcination temperature on the catalytic activity is displayed in Figure S3, which reveals that the calcination temperature has a crucial effect on the SCR activity. The NO conversion on the Mn_xCe_y mixed oxide catalyst is in the order Mn_1Ce_1-500 °C > Mn_1Ce_1-450 °C > Mn_1Ce_1-300 °C > Mn_1Ce_1-400 °C > Mn_1Ce_1-550 °C > Mn_1Ce_1-350 °C. The best calcined temperature is 500 °C. Meanwhile, Table S1 presents that the SCR performance of the Mn_1Ce_1 catalyst is comparable to those of other various metal-substituted catalysts reported in the literature.

Also, the result of N_2 selectivity is tested and shown in Figure 8b. The Mn_1Ce_1 catalyst presents a relatively high N_2 selectivity above 80% in the range of 60−220 °C, which

https://doi.org/10.1021/acsomega.1c01123
ACS Omega 2021, 6, 12801−12812

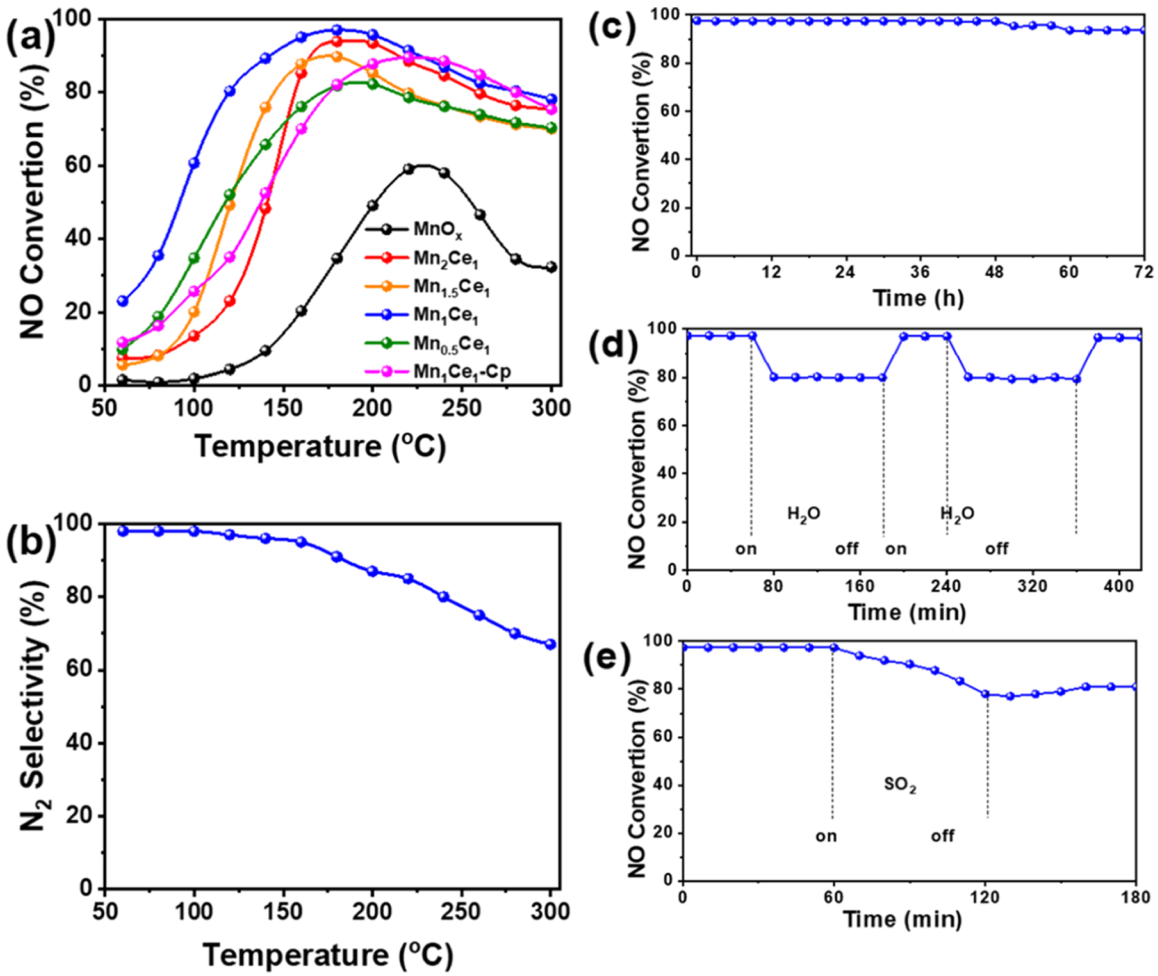

Figure 8. NH_3-SCR activity of (a) de-NO_x performance, (b) N_2 selectivity of Mn_1Ce_1, (c) stability test of Mn_1Ce_1, (d)H_2O resistance of Mn_1Ce_1, and (e) SO_2 resistance of Mn_1Ce_1. Reaction condition: 500 ppm NH_3, 500 ppm NO, 5 vol % O_2, with N_2 as balance gas, and GHSV 38,000 h^{-1}.

slightly decreases at high temperature. The increase of intermediate product NH_4NO_3 in NH_3-SCR reaction may be the main reason for this phenomenon. Both the higher NO conversion and N_2 selectivity of Mn_1Ce_1 demonstrate its better de-NO_x performance. The catalytic stability of the Mn_1Ce_1 catalyst is displayed in Figure 8c. At 180 °C, the NO_x conversion of Mn_1Ce_1 can maintain above 95% after 70 h, indicating a good catalytic stability, which is a very important factor for practical application.

In the process of NH_3-SCR reaction, the presence of water vapor affects the catalytic activity. Therefore, the effect of water vapor on Mn_1Ce_1 catalytic performance was explored. As shown in Figure 8d, the conversion of Mn_1Ce_1 catalyst decreases to 80% when 5% water is introduced at 180 °C, indicating that the presence of water vapor has a negative effect on the active sites of the sample, which could block active sites on the catalyst surface. After closing the steam inlet, the conversion of the catalyst quickly recovered to about 97%, which suggests that the effect of water on the NH_3-SCR activity of the 3D binary metal oxide is reversible. In order to investigate the SO_2 poisoning process during catalytic oxidation of NO, the Mn_1Ce_1 catalyst was tested, and the results are shown in Figure 8e. The de-NO_x ability remains at 97% for 60 min before SO_2 gas is introduced. When SO_2 is added to the simulated fumes, the catalytic activity decreases simultaneously with reaction time. After 60 min of injection, the SO_2 gas is stopped, and NO conversion declines from 97 to 75%. The catalytic activity is restored to 82% after cutting off SO_2 for 60 min, indicating that SO_2 leads to slight deactivation of the catalyst for NH_3-SCR. This phenomenon is possibly ascribed to the sulfation (e.g., formation of $(NH_4)_2SO_4$ and NH_4HSO_4) and the accumulation of sulfates with active species (such as $Ce_2(SO_4)_3$, $Ce(SO_4)_2$, and/or $MnSO_4$), which induce the blocking of active sites or catalyst pores.[61−63]

3.3. In Situ DRIFTS. *3.3.1. NH_3 Adsorption.* The chemical adsorption of NH_3 on MnO_x and Mn_1Ce_1 catalysts at different temperatures was studied by in situ FTIR spectroscopy. Figure 9a shows the DRIFT spectra of NH_3 on MnO_x at different temperatures. Five NH_3 adsorption bands could be detected at 1572, 1525, 1434, 1346, and 1255 cm^{-1}, respectively. These bands include the NH_3 species adsorbed on the Lewis acid sites (1572, 1346, and 1255 cm^{-1}), NH_4^+ species linked to Brønsted acid sites (1434 cm^{-1}), and NH_2 species (1525 cm^{-1}).[64−66] The peak intensity gradually decreases with increasing temperature, suggesting that the adsorption of NH_3 species is unstable. Similarly, different NH_3 adsorption peaks are observed on the Mn_1Ce_1 catalyst surface in Figure 9b. The NH_2 species appear at 1552 and 1525 cm^{-1}.[67] The absorption peaks of NH_4^+ species at Brønsted acid sites appear at 1465 and 1383 cm^{-1}, while the bands at 1327 and 1233 cm^{-1} are assigned to the coordinated NH_3 on the Lewis acid sites. Based on the results obtained from NH_3-TPD, NH_3 can

https://doi.org/10.1021/acsomega.1c01123
ACS Omega 2021, 6, 12801−12812

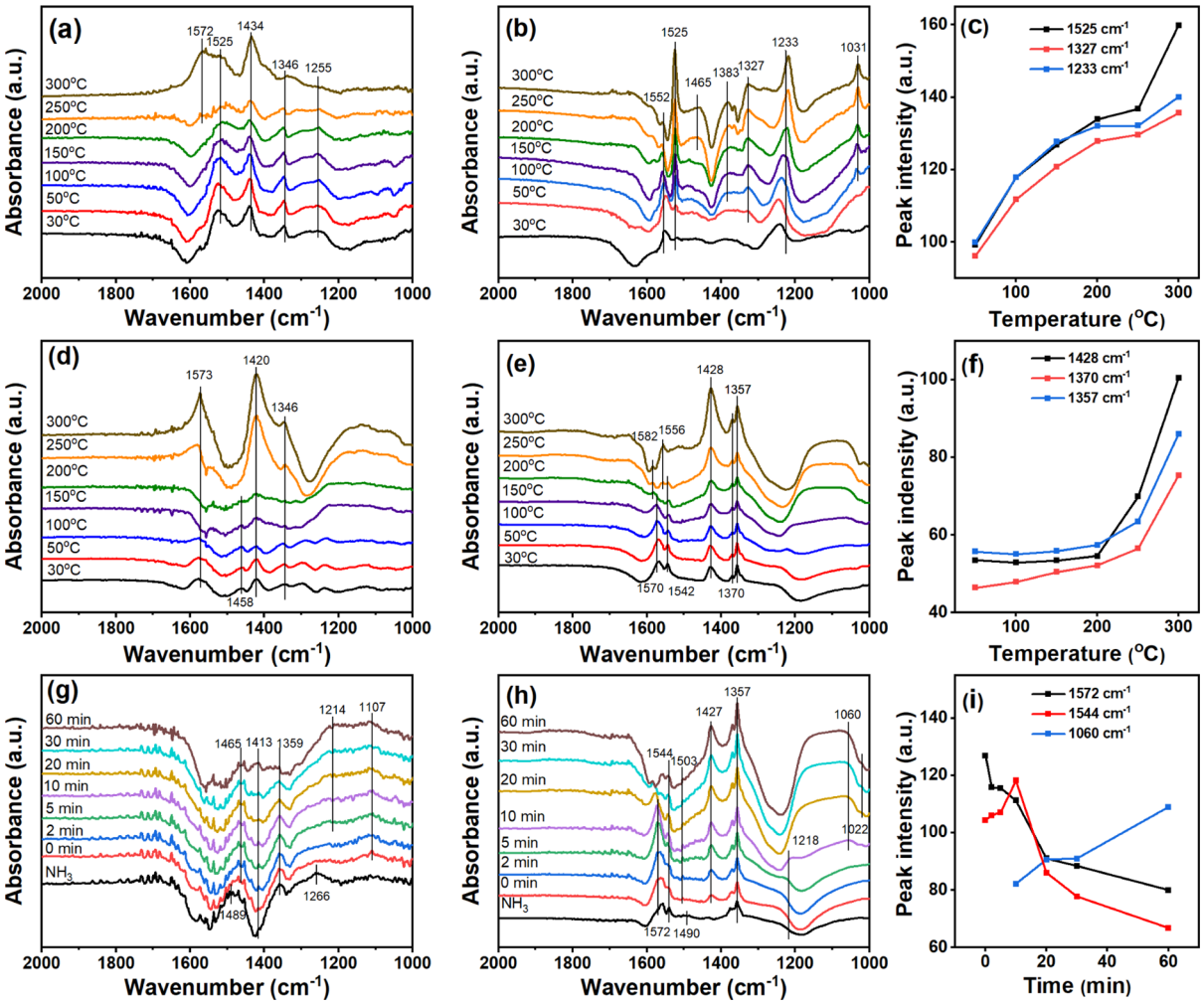

Figure 9. NH_3 adsorption DRIFT spectra over (a) MnO_x and (b,c) Mn_1Ce_1; NO + O_2 adsorption DRIFT spectra over (d) MnO_x and (e,f) Mn_1Ce_1; and transient reaction of NO_x with pre-adsorbed NH_3 over (g) MnO_x and (h,i) Mn_1Ce_1.

be adsorbed on different active sites, so Brønsted acid sites and Lewis acid sites coexist on the sample surface, which can be observed on both two samples. Moreover, it can be seen from Table 2 that Mn_1Ce_1 generates more NH_3 adsorption sites due to its larger surface. Therefore, stronger adsorption and activation ability of NH_3 on the catalyst surface results in enhanced band intensities in Figure 9b. The typical peaks for Mn_1Ce_1 all increase with the increasing temperature, suggesting an enhanced reactivity of NH_3 (Figure 9c).

3.3.2. NO + O_2 Adsorption. The steady-state adsorption spectra of NO + O_2 for MnO_x and Mn_1Ce_1 catalysts show nearly the same variation in Figure 9d,e. For MnO_x, the peaks at 1346 and 1420 cm^{-1} belong to the species of *cis*-$N_2O_2^{2-}$ and *trans*-$N_2O_2^{2-}$, respectively.[68,69] The peak at 1560−1585 cm^{-1} is attributed to the absorption peak of the bidentate nitrate species, while the peak detected at 1458 cm^{-1} is related to monodentate nitrite.[16] For Mn_1Ce_1, the peaks assigned to *cis*-$N_2O_2^{2-}$ (1357 cm^{-1}), *trans*-$N_2O_2^{2-}$ (1428 cm^{-1}), bidentate nitrate (1370, 1570, and 1582 cm^{-1}) and monodentate nitrite (1542 and 1556 cm^{-1}) become more intensive. Figure 9f indicates that the addition of CeO_2 promotes the formation of various intermediate nitrate and nitrite species. More $N_2O_2^{2-}$, bidentate nitrate, and monodentate nitrite species on the surface of Mn_1Ce_1 may improve the NH_3-SCR activity.

3.3.3. Reactions between NO + O_2 and Adsorbed NH_3 Species. The reactivity of NO + O_2 species with pre-adsorbed NH_3 was also studied on MnO_x and Mn_1Ce_1 catalysts by use of in situ DRIFTS at 180 °C, which was measured as a function of time (Figure 9g,h). As shown in Figure 9g, when the reaction gas is converted to NO + O_2, the peak intensity of all NH_3-adsorbed species on MnO_x does not change much. The bands at 1489, 1465, and 1413 cm^{-1} can be assigned to the NH_4^+ species adsorbed on Brønsted acid sites, while the band at 1359 cm^{-1} could be attributed to NH_3 coordinated to Lewis acid sites. The band at 1266 cm^{-1} is detected for NH_2 species. Two new bands attributed to nitrate products at 1214 and 1107 cm^{-1} are detected, suggesting that both NH_4^+ and coordinated NH_3 on the MnO_x surface could react with gaseous NO_x.

For Mn_1Ce_1, after introducing NO + O_2, the bands attributed to NH_4^+ species at 1490 cm^{-1} and ascribed to coordinated NH_3 at 1572 and 1218 cm^{-1} decrease in intensity as displayed in Figure 9h. The band due to NH_2 species at 1544 cm^{-1} increases first and then decreases as the reaction goes on. Moreover, several bands (1022, 1060, and 1503 cm^{-1}) attributed to nitrate products appear. Based on Figure 9g,h, the amount of adsorbed NH_3 and nitrate species on Mn_1Ce_1 surface are higher than that on MnO_x surface, suggesting that the addition of CeO_2 to MnO_x could produce

https://doi.org/10.1021/acsomega.1c01123
ACS Omega 2021, 6, 12801−12812

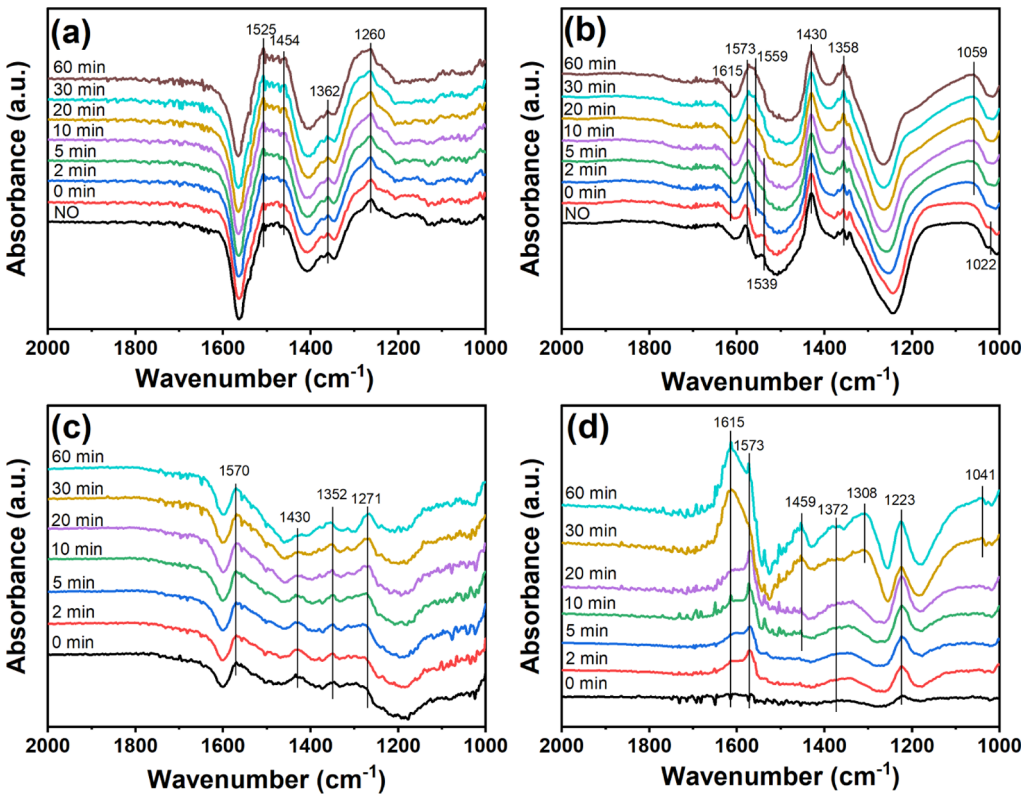

Figure 10. Transient reaction of NH_3 with pre-adsorbed NO + O_2 over (a) MnO_x and (b) Mn_1Ce_1 and coadsorption/reaction of NH_3, NO, and O_2 over (c) MnO_x and (d) Mn_1Ce_1.

more coordinated NH_3 and ionic NH_4^+ and enhance the low-temperature activity. As mentioned above, the adsorbed NH_3 on both Lewis and Brønsted acid sites and gaseous NO species are the major characteristics in the transient SCR reaction, following the applicability of the Eley−Rideal (E−R) mechanism for it.[70]

3.3.4. Reactions between NH_3 and Adsorbed NO + O_2 Species. The reactivity of the pre-absorbed NO_x species on catalysts in the SCR catalytic reaction was further studied. For MnO_x, it can be seen from Figure 10a that after introduction of NH_3, the peaks of monodentate nitrate at 1525 and 1454 cm^{-1}, the *cis*-$N_2O_2^{2-}$ species at 1362 cm^{-1}, and the bidentate nitrate species at 1260 cm^{-1} are nearly unchanged, which indicates that the above-mentioned nitrate species hardly participate in the NH_3-SCR reaction on MnO_x. Figure 10b displays the in situ DRIFT spectra for NH_3 and adsorbed NO + O_2 over Mn_1Ce_1 at 180 °C for different times. After the adsorption of NO + O_2, the surface of Mn_1Ce_1 is mainly covered by *trans*-$N_2O_2^{2-}$ (at 1430 cm^{-1}), *cis*-$N_2O_2^{2-}$ (at 1022 and 1358 cm^{-1}), bidentate nitrate (at 1573 cm^{-1}), and monodentate nitrite (at 1539 cm^{-1}). After the further introduction of NH_3, the bands of monodentate nitrite and *cis*-$N_2O_2^{2-}$ decrease and disappear in 2 min. At the same time, the bands at 1059 and 1559 cm^{-1} attributed to nitrate products and coordinated NH_3 at 1615 cm^{-1} appear after 2 min, indicating that monodentate nitrite and *cis*-$N_2O_2^{2-}$ are reactive in the NH_3-SCR reaction. On the contrary, the other pre-adsorbed NO_x species over the catalyst sample is still present after the introduction of NH_3, suggesting the NH_3-SCR reactivity over these species through the Langmuir−Hinshelwood (L−H) mechanism is low.[70]

3.3.5. DRIFT Spectra in a Flow of NO + NH_3 + O_2. In order to identify the substances present in the catalyst and the reaction, the in situ DRIFT spectrum was recorded with a flow of NO + NH_3 + O_2 at a reaction temperature of 180 °C. As shown in Figure 10c, bands assigning to NH_3 coordinated on Lewis acid (1352 cm^{-1}), *trans*-$N_2O_2^{2-}$ (1430 cm^{-1}), and the nitrate species (1271 cm^{-1}) from NO adsorption are all detected on the MnO_x surface. At the same time, bands for NH_4^+ ions formed due to the H_2O production (1459 cm^{-1}), bidentate nitrate (1573 cm^{-1}), coordinated NH_3 (1223 cm^{-1}), and nitrate species (1308 and 1615 cm^{-1}) also appear in Figure 10d. However, the peak intensity of Mn_1Ce_1 is more obvious, suggesting that the presence of Ce enhances both the adsorption and activation of NH_3 and NO species on the catalyst. From the research above, the following results can be obtained. During the SCR reaction, the E−R mechanism plays a vital part in the SCR processes over catalysts; the addition of Ce brings in more acid sites, which is positive for the adsorption of NH_3 species.[71] In addition, the interaction between Ce and Mn results in the enhanced surface area and the highly dispersed MnO_x active sites and thus improve the low-temperature activity.

As discussed above, all the ad-NO species in the transient SCR reaction only has a much lower reactivity, indicating that there is a blockage on the NH_3-SCR reactions over Mn_xCe_y catalysts through the L−H pathway. Meanwhile, the reaction intermediate NH_2 is observed, demonstrating the occurrence of the E−R mechanism. The SCR reaction through the E−R mechanism can be described as[72]

$$NH_3(g) + Mn^{4+}/Ce^{3+} \rightarrow NH_3(ad) + Mn^{3+}/Ce^{4+} \quad (1)$$

$$O_2(g) \rightarrow 2O(ad) \quad (2)$$

https://doi.org/10.1021/acsomega.1c01123
ACS Omega 2021, 6, 12801−12812

$$NH_3(ad) + O(ad) \rightarrow NH_2(ad) + OH(ad) \quad (3)$$

$$NH_2(ad) + NO(g) \rightarrow N_2 + H_2O \quad (4)$$

The possible reaction pathway for selective catalytic reduction of NO with NH_3 over the Mn_xCe_y catalysts is proposed in Figure 11. First, the gas NH_3 is adsorbed on Lewis acid sites and Brønsted acid sites in the form of NH_4^+ ions and coordinated NH_3 on the catalyst surface (reaction 1), whereas the reactant NO is still in the gas phase or form the weakly adsorbed state. Then, the adsorbed NH_3 species could react with O_2 easily to produce NH_2 (reaction 3). At last, the NH_2 rapidly react with NO to generate N_2 and H_2O.

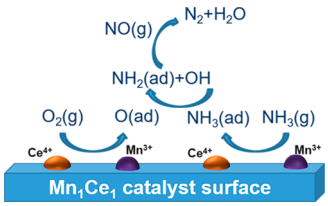

Figure 11. Proposed reaction mechanism of NH_3-SCR of NO over a Mn_1Ce_1 catalyst surface.

4. CONCLUSIONS

In summary, a Mn_xCe_y binary mixed oxide network with a 3D structure is prepared by using the polymer-assisted chemical solution method. Due to the effect of static electricity and hydrogen bonding, EDTA and the stable macromolecular chain of PEI form a "metal ion-EDTA-PEI" homogeneous precursor solution with an initial network structure. During the calcination, EDTA and PEI decompose to gaseous substances and escape, and the 3D network is retained at the same time. The network has a favorable mesoporous structure, which facilitates the diffusion of the reaction gas and the exposure of active sites of the catalyst. The co-doped cerium serves as an oxygen supply center for active oxygen transport. Thus, the binary mixed oxide network possesses rich active oxygen species and much more acid sites. The NO_x conversion of the Mn_1Ce_1 catalyst exhibits 97% at 180 °C and maintains above 95% after 70 h, which is comparable to some other various metal-substituted catalysts. The in situ DRIFTS studies reveal that the E−R route between gaseous NO and adsorbed NH_3 is dominant in the catalytic reaction of Mn_xCe_y binary catalysts. Therefore, the Mn_1Ce_1 catalyst prepared by the polymer-assisted deposition method for the first time presents broad application prospects in various catalytic reactions and probably becomes a potential alternative to NH_3-SCR of NO under low-temperature conditions.

■ ASSOCIATED CONTENT

Supporting Information

The Supporting Information is available free of charge at https://pubs.acs.org/doi/10.1021/acsomega.1c01123.

Raman spectra of Mn_xCe_y binary mixed oxide catalysts; N_2 adsorption−desorption isotherms and BJH pore size distribution of Mn_xCe_y catalysts; effect of calcination temperature on the catalytic activity; and comparison of NO_x reduction performance (PDF)

■ AUTHOR INFORMATION

Corresponding Authors

Jitong Wang − *State Key Laboratory of Chemical Engineering, East China University of Science and Technology, Shanghai 200237, China; Key Laboratory of Specially Functional Polymeric Materials and Related Technology, East China University of Science and Technology, Shanghai 200237, China;* orcid.org/0000-0001-8557-6743; Email: wangjt@ecust.edu.cn

Wenming Qiao − *State Key Laboratory of Chemical Engineering, East China University of Science and Technology, Shanghai 200237, China; Key Laboratory of Specially Functional Polymeric Materials and Related Technology, East China University of Science and Technology, Shanghai 200237, China;* orcid.org/0000-0002-8114-684X; Email: qiaowm@ecust.edu.cn

Authors

Xixi Xiao − *State Key Laboratory of Chemical Engineering, East China University of Science and Technology, Shanghai 200237, China*

Xianfeng Jia − *State Key Laboratory of Chemical Engineering, East China University of Science and Technology, Shanghai 200237, China; Department of Chemistry, Tangshan Normal University, Tangshan 063000, China*

Cheng Ma − *State Key Laboratory of Chemical Engineering, East China University of Science and Technology, Shanghai 200237, China*

Licheng Ling − *State Key Laboratory of Chemical Engineering, East China University of Science and Technology, Shanghai 200237, China; Key Laboratory of Specially Functional Polymeric Materials and Related Technology, East China University of Science and Technology, Shanghai 200237, China;* orcid.org/0000-0002-1691-2026

Complete contact information is available at: https://pubs.acs.org/10.1021/acsomega.1c01123

Notes

The authors declare no competing financial interest.

■ ACKNOWLEDGMENTS

This work was financially supported by the National Natural Science Foundation of China (no. 21978097 and U1710252), the CAS Key Laboratory of Carbon Materials (no. KLCMKFJJ2001), and the Fundamental Research Funds for the Central Universities (222201817001, 50321041918013, and 50321042017001).

■ REFERENCES

(1) Skalska, K.; Miller, J. S.; Ledakowicz, S. Trends in $NO_{(x)}$ abatement: a review. *Sci. Total Environ.* **2010**, *408*, 3976−3989.

(2) Yu, Y.; Chen, C.; Ma, M.; Douthwaite, M.; He, C.; Miao, J.; Chen, J.; Li, C. SO_2 promoted in situ recovery of thermally deactivated $Fe_2(SO_4)_3/TiO_2$ NH_3-SCR catalysts: from experimental work to theoretical study. *Chem. Eng. J.* **2019**, *361*, 820−829.

(3) Yu, J.; Guo, F.; Wang, Y.; Zhu, J.; Liu, Y.; Su, F.; Gao, S.; Xu, G. Sulfur poisoning resistant mesoporous Mn-base catalyst for low-temperature SCR of NO with NH_3. *Appl. Catal., B* **2010**, *95*, 160−168.

(4) You, X.; Sheng, Z.; Yu, D.; Yang, L.; Xiao, X.; Wang, S. Influence of Mn/Ce ratio on the physicochemical properties and catalytic performance of graphene supported MnO_x-CeO_2 oxides for NH_3-SCR at low temperature. *Appl. Surf. Sci.* **2017**, *423*, 845−854.

(5) Yang, Y.; Liu, J.; Liu, F.; Wang, Z.; Ding, J.; Huang, H. Reaction mechanism for NH_3-SCR of NO_x over $CuMn_2O_4$ catalyst. *Chem. Eng. J.* **2019**, *361*, 578−587.
(6) Yang, Y.; Bu, W.; Im, S.; Meagher, J.; Stuckey, J.; Waskell, L. Structure of cytochrome P450 2B4 with an acetate ligand and an active site hydrogen bond network similar to oxyferrous P450cam. *J. Inorg. Biochem.* **2018**, *185*, 17−25.
(7) Yang, N.-z.; Guo, R.-t.; Pan, W.-g.; Chen, Q.-l.; Wang, Q.-s.; Lu, C.-z. The promotion effect of Sb on the Na resistance of Mn/TiO_2 catalyst for selective catalytic reduction of NO with NH_3. *Fuel* **2016**, *169*, 87−92.
(8) Jiang, L.; Liu, Q.; Ran, G.; Kong, M.; Ren, S.; Yang, J.; Li, J. V_2O_5-modified Mn-Ce/AC catalyst with high SO_2 tolerance for low-temperature NH_3-SCR of NO. *Chem. Eng. J.* **2019**, *370*, 810−821.
(9) Dahlin, S.; Nilsson, M.; Bäckström, D.; Bergman, S. L.; Bengtsson, E.; Bernasek, S. L.; Pettersson, L. J. Multivariate analysis of the effect of biodiesel-derived contaminants on V_2O_5-WO_3/TiO_2 SCR catalysts. *Appl. Catal., B* **2016**, *183*, 377−385.
(10) Thirupathi, B.; Smirniotis, P. G. Nickel-doped Mn/TiO_2 as an efficient catalyst for the low-temperature SCR of NO with NH_3: catalytic evaluation and characterizations. *J. Catal.* **2012**, *288*, 74−83.
(11) Sheng, Z.; Hu, Y.; Xue, J.; Wang, X.; Liao, W. SO_2 poisoning and regeneration of Mn-Ce/TiO_2 catalyst for low temperature NO_x reduction with NH_3. *J. Rare Earths* **2012**, *30*, 676−682.
(12) Shen, B.; Liu, T.; Zhao, N.; Yang, X.; Deng, L. Iron-doped Mn-Ce/TiO_2 catalyst for low temperature selective catalytic reduction of NO with NH_3. *J. Environ. Sci.* **2010**, *22*, 1447−1454.
(13) Putluru, S. S. R.; Schill, L.; Jensen, A. D.; Siret, B.; Tabaries, F.; Fehrmann, R. Mn/TiO_2 and Mn-Fe/TiO_2 catalysts synthesized by deposition precipitation-promising for selective catalytic reduction of NO with NH_3 at low temperatures. *Appl. Catal., B* **2015**, *165*, 628−635.
(14) Sun, C.; Liu, H.; Chen, W.; Chen, D.; Yu, S.; Liu, A.; Dong, L.; Feng, S. Insights into the Sm/Zr co-doping effects on N_2 selectivity and SO_2 resistance of a MnO_x-TiO_2 catalyst for the NH_3-SCR reaction. *Chem. Eng. J.* **2018**, *347*, 27−40.
(15) Song, L.; Chao, J.; Fang, Y.; He, H.; Li, J.; Qiu, W.; Zhang, G. Promotion of ceria for decomposition of ammonia bisulfate over V_2O_5-MoO_3/TiO_2 catalyst for selective catalytic reduction. *Chem. Eng. J.* **2016**, *303*, 275−281.
(16) Niu, Y.; Shang, T.; Hui, S.; Zhang, X.; Lei, Y.; Lv, Y.; Wang, S. Synergistic removal of NO and N_2O in low-temperature SCR process with MnO_x/Ti based catalyst doped with Ce and V. *Fuel* **2016**, *185*, 316−322.
(17) Liu, J.; Liu, J.; Zhao, Z.; Tan, J.; Wei, Y.; Song, W. Fe/Beta@SBA-15 core-shell catalyst: Interface stable effect and propene poisoning resistance for no abatement. *AIChE J.* **2018**, *64*, 3967−3978.
(18) Liu, J.; Liu, J.; Zhao, Z.; Wei, Y.; Song, W. Fe-Beta@CeO_2 core-shell catalyst with tunable shell thickness for selective catalytic reduction of NO_x with NH_3. *AIChE J.* **2017**, *63*, 4430−4441.
(19) Liu, J.; Zhao, Z.; Xu, C.; Liu, J. Structure, synthesis, and catalytic properties of nanosize cerium-zirconium-based solid solutions in environmental catalysis. *Chin. J. Catal.* **2019**, *40*, 1438−1487.
(20) Xie, A.; Tang, Y.; Huang, X.; Jin, X.; Gu, P.; Luo, S.; Yao, C.; Li, X. Three-dimensional nanoflower MnCrO/Sepiolite catalyst with increased SO_2 resistance for NH_3-SCR at low temperature. *Chem. Eng. J.* **2019**, *370*, 897−905.
(21) Ren, D.; Gui, K. Study of the adsorption of NH_3 and NO_x on the nano-γFe_2O_3 (001) surface with density functional theory. *Appl. Surf. Sci.* **2019**, *487*, 171−179.
(22) Metkar, P. S.; Harold, M. P.; Balakotaiah, V. Selective catalytic reduction of NO_x on combined Fe- and Cu-zeolite monolithic catalysts: sequential and dual layer configurations. *Appl. Catal., B* **2012**, *111-112*, 67−80.
(23) Zhang, N.; Li, L.; Guo, Y.; He, J.; Wu, R.; Song, L.; Zhang, G.; Zhao, J.; Wang, D.; He, H. A MnO_2-based catalyst with H_2O resistance for NH_3-SCR: study of catalytic activity and reactants-H_2O competitive adsorption. *Appl. Catal., B* **2020**, *270*, 118860.
(24) Yang, J.; Ren, S.; Zhang, T.; Su, Z.; Long, H.; Kong, M.; Yao, L. Iron doped effects on active sites formation over activated carbon supported Mn-Ce oxide catalysts for low-temperature SCR of NO. *Chem. Eng. J.* **2020**, *379*, 122398.
(25) Qi, G.; Yang, R. T.; Chang, R. MnO_x-CeO_2 mixed oxides prepared by co-precipitation for selective catalytic reduction of NO with NH_3 at low temperatures. *Appl. Catal., B* **2004**, *51*, 93−106.
(26) Tang, X.; Hao, J.; Yi, H.; Li, J. Low-temperature SCR of NO with NH_3 over AC/C supported manganese-based monolithic catalysts. *Catal. Today* **2007**, *126*, 406−411.
(27) Yang, S.; Liao, Y.; Xiong, S.; Qi, F.; Dang, H.; Xiao, X.; Li, J. N_2 selectivity of NO reduction by NH_3 over MnO_x-CeO_2: mechanism and key factors. *J. Phys. Chem. C* **2014**, *118*, 21500−21508.
(28) Qi, G.; Yang, R. T. Performance and kinetics study for low-temperature SCR of NO with NH_3 over MnO_x-CeO_2 catalyst. *J. Catal.* **2003**, *217*, 434−441.
(29) Liu, Z.; Yi, Y.; Zhang, S.; Zhu, T.; Zhu, J.; Wang, J. Selective catalytic reduction of NO_x with NH_3 over Mn-Ce mixed oxide catalyst at low temperatures. *Catal. Today* **2013**, *216*, 76−81.
(30) Damma, D.; Ettireddy, P.; Reddy, B.; Smirniotis, P. A review of low temperature NH_3-SCR for removal of NO_x. *Catalysts* **2019**, *9*, 349.
(31) Guo, R.-t.; Chen, Q.-l.; Ding, H.-l.; Wang, Q.-s.; Pan, W.-g.; Yang, N.-z.; Lu, C.-z. Preparation and characterization of CeO_x@MnO_x core-shell structure catalyst for catalytic oxidation of NO. *Catal. Commun.* **2015**, *69*, 165−169.
(32) Liu, J.; Cheng, H.; Bao, J.; Zhang, P.; Liu, M.; Leng, Y.; Zhang, Z.; Tao, R.; Liu, J.; Zhao, Z.; Dai, S. Aluminum hydroxide-mediated synthesis of mesoporous metal oxides by a mechanochemical nanocasting strategy. *J. Mater. Chem. A* **2019**, *7*, 22977−22985.
(33) Cheng, H.; Feng, G.; Yang, Z.; Wang, T.; Okejiri, F.; Tan, J.; Zhao, M.; Liu, J.; Liu, J.; Zhao, Z. Green synthesis of mesoporous $MnNbO_x$ oxide by a liquid induced self-assembly strategy for low-temperature removal of NO_x. *Chem. Commun.* **2019**, *55*, 15073−15076.
(34) Cheng, H.; Tan, J.; Ren, Y.; Zhao, M.; Liu, J.; Wang, H.; Liu, J.; Zhao, Z. Mechanochemical synthesis of highly porous $CeMnO_x$ catalyst for the removal of NO_x. *Ind. Eng. Chem. Res.* **2019**, *58*, 16472−16478.
(35) Burrell, A. K.; Mark McCleskey, T.; Jia, Q. X. Polymer assisted deposition. *Chem. Commun.* **2008**, *11*, 1271−1277.
(36) Jiang, X.; Li, X.; Wang, J.; Long, D.; Ling, L.; Qiao, W. Three-dimensional Mn-Cu-Ce ternary mixed oxide networks prepared by polymer-assisted deposition for HCHO catalytic oxidation. *Catal. Sci. Technol.* **2018**, *8*, 2740−2749.
(37) Li, H.; Wang, Y.; Wang, S.; Wang, X.; Hu, J. Removal of elemental mercury in flue gas at lower temperatures over Mn-Ce based materials prepared by co-precipitation. *Fuel* **2017**, *208*, 576−586.
(38) Yang, S.; Zhang, M.; Wu, X.; Wu, X.; Zeng, F.; Li, Y.; Duan, S.; Fan, D.; Yang, Y.; Wu, X. The excellent electrochemical performances of $ZnMn_2O_4$/Mn_2O_3: the composite cathode material for potential aqueous zinc ion batteries. *J. Electroanal. Chem.* **2019**, *832*, 69−74.
(39) Zhan, S.; Zhang, H.; Zhang, Y.; Shi, Q.; Li, Y.; Li, X. Efficient NH_3-SCR removal of NO_x with highly ordered mesoporous $WO_{3(\chi)}$-CeO_2 at low temperatures. *Appl. Catal., B* **2017**, *203*, 199−209.
(40) Atif, M.; Iqbal, S.; Ismail, M.; Mansoor, Q.; Mughal, L.; Aziz, M. H.; Hanif, A.; Farooq, W. A. Manganese-doped cerium oxide nanocomposite induced photodynamic therapy in MCF-7 cancer cells and antibacterial activity. *BioMed Res. Int.* **2019**, *2019*, 1.
(41) Han, L.; Gao, M.; Hasegawa, J.-y.; Li, S.; Shen, Y.; Li, H.; Shi, L.; Zhang, D. SO_2-tolerant selective catalytic reduction of NO_x over meso-TiO_2@Fe_2O_3@Al_2O_3 metal-based monolith catalysts. *Environ. Sci. Technol.* **2019**, *53*, 6462−6473.
(42) Kim, H. J.; Lee, G.; Jang, M. G.; Noh, K. J.; Han, J. W. Rational design of transition metal Co-doped ceria catalysts for low-temperature CO oxidation. *ChemCatChem* **2019**, *11*, 2288−2296.

https://doi.org/10.1021/acsomega.1c01123
ACS Omega 2021, 6, 12801−12812

(43) Han, Y.-F.; Ramesh, K.; Chen, L.; Widjaja, E.; Chilukoti, S.; Chen, F. Observation of the reversible phase-transformation of α-Mn_2O_3 nanocrystals during the catalytic combustion of methane by in situ Raman spectroscopy. *J. Phys. Chem. C* **2007**, *111*, 2830−2833.
(44) Fazio, B.; Spadaro, L.; Trunfio, G.; Negro, J.; Arena, F. Raman scattering of MnO_x-CeO_x composite catalysts: structural aspects and laser-heating effects. *J. Raman Spectrosc.* **2011**, *42*, 1583−1588.
(45) Zheng, Y.; Wang, W.; Jiang, D.; Zhang, L. Amorphous MnO_x modified Co_3O_4 for formaldehyde oxidation: improved low-temperature catalytic and photothermocatalytic activity. *Chem. Eng. J.* **2016**, *284*, 21−27.
(46) Xu, J.; Li, P.; Song, X.; He, C.; Yu, J.; Han, Y.-F. Operando raman spectroscopy for determining the active phase in one-dimensional $Mn_{1-x}Ce_xO_{2\pm y}$ nanorod catalysts during methane combustion. *J. Phys. Chem. Lett.* **2010**, *1*, 1648−1654.
(47) Poyraz, A. S.; Song, W.; Kriz, D.; Kuo, C.-H.; Seraji, M. S.; Suib, S. L. Crystalline mesoporous $K_{2-x}Mn_8O_{16}$ and ε-MnO_2 by mild transformations of amorphous mesoporous manganese oxides and their enhanced redox properties. *ACS Appl. Mater. Interfaces* **2014**, *6*, 10986−10991.
(48) Cao, F.; Xiang, J.; Su, S.; Wang, P.; Sun, L.; Hu, S.; Lei, S. The activity and characterization of MnO_x-CeO_2-ZrO_2/γ-Al_2O_3 catalysts for low temperature selective catalytic reduction of NO with NH_3. *Chem. Eng. J.* **2014**, *243*, 347−354.
(49) Kong, M.; Liu, Q.; Wang, X.; Ren, S.; Yang, J.; Zhao, D.; Xi, W.; Yao, L. Performance impact and poisoning mechanism of arsenic over commercial V_2O_5-WO_3/TiO_2 SCR catalyst. *Catal. Commun.* **2015**, *72*, 121−126.
(50) Chen, H.; Xia, Y.; Huang, H.; Gan, Y.; Tao, X.; Liang, C.; Luo, J.; Fang, R.; Zhang, J.; Zhang, W.; Liu, X. Highly dispersed surface active species of Mn/Ce/TiW catalysts for high performance at low temperature NH_3-SCR. *Chem. Eng. J.* **2017**, *330*, 1195−1202.
(51) Andersen, N. I.; Serov, A.; Atanassov, P. Metal oxides/CNT nano-composite catalysts for oxygen reduction/oxygen evolution in alkaline media. *Appl. Catal., B* **2015**, *163*, 623−627.
(52) Delimaris, D.; Ioannides, T. VOC oxidation over MnO_x-CeO_2 catalysts prepared by a combustion method. *Appl. Catal., B* **2008**, *84*, 303−312.
(53) Arena, F.; Trunfio, G.; Negro, J.; Fazio, B.; Spadaro, L. Basic evidence of the molecular dispersion of $MnCeO_x$ catalysts synthesized via a novel "redox-precipitation" route. *Chem. Mater.* **2007**, *19*, 2269−2276.
(54) Chen, L.; Weng, D.; Wang, J.; Weng, D.; Cao, L. Low-temperature activity and mechanism of WO_3-modified CeO_2-TiO_2 catalyst under NH_3-NO/NO_2 SCR conditions. *Chin. J. Catal.* **2018**, *39*, 1804−1813.
(55) Fan, J.; Ning, P.; Song, Z.; Liu, X.; Wang, L.; Wang, J.; Wang, H.; Long, K.; Zhang, Q. Mechanistic aspects of NH_3-SCR reaction over CeO_2/TiO_2-ZrO_2-SO_4^{2-} catalyst: in situ DRIFTS investigation. *Chem. Eng. J.* **2018**, *334*, 855−863.
(56) Zhou, X.; Huang, X.; Xie, A.; Luo, S.; Yao, C.; Li, X.; Zuo, S. V_2O_5-decorated Mn-Fe/attapulgite catalyst with high SO_2 tolerance for SCR of NO_x with NH_3 at low temperature. *Chem. Eng. J.* **2017**, *326*, 1074−1085.
(57) Shan, W.; Liu, F.; He, H.; Shi, X.; Zhang, C. A superior Ce-W-Ti mixed oxide catalyst for the selective catalytic reduction of NO_x with NH_3. *Appl. Catal., B* **2012**, *115-116*, 100−106.
(58) Peng, Y.; Li, K.; Li, J. Identification of the active sites on CeO_2-WO_3 catalysts for SCR of NO_x with NH_3: an in situ IR and Raman spectroscopy study. *Appl. Catal., B* **2013**, *140-141*, 483−492.
(59) Boningari, T.; Ettireddy, P. R.; Somogyvari, A.; Liu, Y.; Vorontsov, A.; McDonald, C. A.; Smirniotis, P. G. Influence of elevated surface texture hydrated titania on Ce-doped Mn/TiO_2 catalysts for the low-temperature SCR of NO under oxygen-rich conditions. *J. Catal.* **2015**, *325*, 145−155.
(60) Kang, L.; Han, L.; He, J.; Li, H.; Yan, T.; Chen, G.; Zhang, J.; Shi, L.; Zhang, D. Improved NO_x reduction in the presence of SO_2 by using Fe_2O_3-promoted halloysite-supported CeO_2-WO_3 catalysts. *Environ. Sci. Technol.* **2019**, *53*, 938−945.
(61) Wang, X.; Du, X.; Zhang, L.; Chen, Y.; Yang, G.; Ran, J. Promotion of NH_4HSO_4 decomposition in NO/NO_2 contained atmosphere at low temperature over V_2O_5-WO_3/TiO_2 catalyst for NO reduction. *Appl. Catal., A* **2018**, *559*, 112−121.
(62) Zhang, L.; Qu, H.; Du, T.; Ma, W.; Zhong, Q. H_2O and SO_2 tolerance, activity and reaction mechanism of sulfated Ni-Ce-La composite oxide nanocrystals in NH_3-SCR. *Chem. Eng. J.* **2016**, *296*, 122−131.
(63) Wu, Z.; Jiang, B.; Liu, Y.; Wang, H.; Jin, R. DRIFT study of manganese/titania-based catalysts for low-temperature selective catalytic reduction of NO with NH_3. *Environ. Sci. Technol.* **2007**, *41*, 5812−5817.
(64) Lian, Z.; Liu, F.; He, H. Enhanced Activity of Ti-Modified V_2O_5/CeO_2 Catalyst for the Selective Catalytic Reduction of NO_x with NH_3. *Ind. Eng. Chem. Res.* **2014**, *53*, 19506−19511.
(65) Yang, N.-z.; Guo, R.-t.; Pan, W.-g.; Chen, Q.-l.; Wang, Q.-s.; Lu, C.-z.; Wang, S.-x. The deactivation mechanism of Cl on Ce/TiO_2 catalyst for selective catalytic reduction of NO with NH_3. *Appl. Surf. Sci.* **2016**, *378*, 513−518.
(66) Chen, J.; Cao, F.; Qu, R.; Gao, X.; Cen, K. Bimetallic cerium-copper nanoparticles embedded in ordered mesoporous carbons as effective catalysts for the selective catalytic reduction of NO with NH_3. *J. Colloid Interface Sci.* **2015**, *456*, 66−75.
(67) Liu, Z.; Zhu, J.; Li, J.; Ma, L.; Woo, S. I. Novel Mn-Ce-Ti mixed-oxide catalyst for the selective catalytic reduction of NO_x with NH_3. *ACS Appl. Mater. Interfaces* **2014**, *6*, 14500−14508.
(68) Liu, Z.; Lu, Y.; Yuan, L.; Ma, L.; Zheng, L.; Zhang, J.; Hu, T. Selective catalytic reduction of NO_x with H_2 over WO_3 promoted Pt/TiO_2 catalyst. *Appl. Catal., B* **2016**, *188*, 189−197.
(69) Chen, Y.; Wang, J.; Yan, Z.; Liu, L.; Zhang, Z.; Wang, X. Promoting effect of Nd on the reduction of NO with NH_3 over CeO_2 supported by activated semi-coke: an in situ DRIFTS study. *Catal. Sci. Technol.* **2015**, *5*, 2251−2259.
(70) Liu, J.; Guo, R.-t.; Li, M.-y.; Sun, P.; Liu, S.-m.; Pan, W.-g.; Liu, S.-w.; Sun, X. Enhancement of the SO_2 resistance of Mn/TiO_2 SCR catalyst by Eu modification: a mechanism study. *Fuel* **2018**, *223*, 385−393.
(71) Peng, Y.; Li, J.; Chen, L.; Chen, J.; Han, J.; Zhang, H.; Han, W. Alkali metal poisoning of a CeO_2-WO_3 catalyst used in the selective catalytic reduction of NO_x with NH_3: an experimental and theoretical study. *Environ. Sci. Technol.* **2012**, *46*, 2864−2869.
(72) Hu, H.; Cai, S.; Li, H.; Huang, L.; Shi, L.; Zhang, D. Mechanistic aspects of deNO_x processing over TiO_2 supported Co-Mn oxide catalysts: structure-activity relationships and in situ DRIFTs analysis. *ACS Catal.* **2015**, *5*, 6069−6077.

https://doi.org/10.1021/acsomega.1c01123
ACS Omega 2021, 6, 12801−12812